

A lattice Boltzmann method for viscous free surface waves in two dimensions

Zhuangming Zhao¹, Ping Huang^{1,*}, Yineng Li² and Junmin Li²

¹*Department of Environmental Science, School of Environmental Science and Engineering, Sun Yat-sen University, Guangzhou 510275, China*

²*State Key Laboratory of Tropical Oceanography, South China Sea Institute of Oceanology, Chinese Academy of Sciences, Guangzhou 510301, China*

SUMMARY

We propose a new method based on the combination of the lattice Boltzmann equation (LBE) and the kinematic boundary condition (KBC) method to simulate viscous free surface wave in two dimensions. In our method, the flow field is modeled by LBE, whereas the free surface is explicitly tracked by the local height function, which is calculated by the KBC method. The free surface boundary condition (FSBC) for LBE is revised from previous researches. Interpolation-supplemented lattice Boltzmann (ISLB) method is introduced, which enables our approach to be applied on arbitrary, nonuniform mesh grids. Five cases are simulated respectively to validate the LBE–KBC method: the stationary flow and the solitary waves simulated by the revised-FSBC are more accurate than the one obtained by the former-FSBC; numerical results of standing waves show that our method is compatible to the existing two-dimensional finite-volume scheme; cases of small amplitude Stokes wave and waves traveling over a submerged bar show good agreement on wave celerity, wavelength, wave amplitude and wave period between numerical results and corresponding analytical solutions and/or experiment data. Copyright © 2012 John Wiley & Sons, Ltd.

Received 11 June 2011; Revised 3 December 2011; Accepted 31 January 2012

KEY WORDS: lattice Boltzmann equation (LBE); kinematic boundary condition (KBC); free surface; viscous wave; non-hydrostatic pressure; multi-relaxation-time (MRT) model

1. INTRODUCTION

Simulations of ocean waves in wave channels are important for ocean science and engineering. To carry out the wave modeling, there are mainly three types of approaches. The first are the depth-integrated models, for example, the standard Boussinesq equation [1] for weakly non-linear shallow-water waves or the classical mild-slope equation [2] for linear waves. To extend the applicability of depth-integrated models, many efforts have been made, that is, the modified Boussinesq models for deeper water [3–8] or the non-linear mild slope models [9–11]. The second is developed on the basis of the inviscid and irrotational flow assumption, for example, the Laplace equation and the nonlinear free surface boundary conditions are usually solved by the boundary element method [12–14]. The Laplace equation has the ability to simulate surface waves without limitations of water depth; however, it cannot describe wave propagation with rotation and energy dissipation owing to the inherent assumptions. The third is the non-hydrostatic model based upon the full Navier–Stokes equations, which involve fluid viscosity. It is the most detailed approach for predicting non-linear dispersive waves, by which the viscosity of fluid and the energy dissipation can be described [15]. Moreover, the wave-induced bottom boundary layer flows, and the shear stresses that act on the

*Correspondence to: Ping Huang, Department of Environmental Science, School of Environmental Science and Engineering, Sun Yat-sen University, Guangzhou 510275, China.

†E-mail: eeshping@mail.sysu.edu.cn

walls can also be simulated. However, the exact kinematic and dynamic boundary conditions at the free surface are also necessary [16, 17], and the accuracy of the approach depends on the calculation of the correct position of the free surface. Therefore, the development of an increasingly accurate and efficient method to simulate viscous free surface waves remains a challenge.

As a newly developing CFD method, the lattice Boltzmann equation (LBE) method has several attractive features: (1) the effectiveness for time-dependent fluid computations; (2) intrinsic parallelism of algorithm, (3) simplicity of programming, and (4) second order accuracy in space and time [18]. It has been successfully applied to the analysis of a variety of complex physical phenomena, such as turbulent flow [19, 20], natural convection [21], advection and dispersion problem [22, 23], multi-component flows [24, 25, 58], and free surface flow [26–29]. For free surface problem, several LBE approaches have been developed. One type of these approaches is the LBE multiphase method. For example, Gunstensen and Rothman [30] proposed a color model for simulating immiscible binary fluids based on a lattice gas model [24]. He *et al.* [31] proposed a lattice Boltzmann scheme for simulation of multiphase flows. Nevertheless, these multiphase models not only increase the amount of calculation but also introduce additional physical variable such as surface tension and diffusive interfaces in the free surface problems. Another type of existing LBE approaches for free surface dynamics are the LBE VOF or LBE VOF-like methods. Körner *et al.* [28] and Thürey *et al.* [27] developed a VOF-like method that the free surface motion is tracked by computing the mass fluxes between the cells, and the change of mass is directly computed from the LBE distribution functions. Moreover, Janssen and Krafczyk [29] proposed a VOF based lattice Boltzmann method, in which they used a VOF method to compute the dynamics of the free surface. Furthermore, a level set based LBE model was proposed by Thürey and Rude [26]. However, the major drawbacks of these VOF or level set LBE method are their tendency to smear the free surface and the high CPU cost because of the need for fine grids and small time steps.

To overcome the weaknesses described earlier, another type of surface tracking techniques using a local height function to define the free surface position can be adopted, to which the depth-integrated continuity (DIC) equation [32, 33] method and kinematic boundary condition (KBC) [34, 35] method belong. The DIC is obtained by integrating the incompressible continuity equation in a liquid column from the bottom to the free surface. Staggered grids are usually used for the stability reasons in DIC method, and it is difficult to be introduced into the LBE, which used a non-staggered grid system. The KBC is the Lagrangian condition that a particle on the surface must remain on the surface. There are mainly two kinds of form: the Lagrangian form and the Eulerian form. It is possible to use the Lagrangian condition directly and advance the free surface by moving marker particles based upon their velocity at the free surface [16, 17, 36]; however, this method has been shown to be unstable in long simulations, where the free-surface is advanced explicitly. Four different forms of the Eulerian KBC are found in literatures: (1) numerical integration of the physical space Eulerian KBC [16, 34, 37–39]; (2) numerical integration of a curvilinear transformation of the physical space Eulerian KBC [40, 41]; (3) rotation of the Cartesian space frame and integration of the physical space Eulerian KBC in a more desirable orientation [42]; and (4) integration of a curvilinear derivation of the KBC [15]. The first two methods are unable to simulate waves which do not remain single valued in the physical space. The third method, rotation of the coordinate system, allows the simulation of a free surface that is multiple valued in physical space; however, the surface must remain single valued in the rotated Cartesian space. The fourth method also allows computation of a free surface that does not remain single valued in physical space coordinates. Furthermore, steepening of the surface wave does not degrade the accuracy of the free surface advance. In this paper, the first method is used for simplicity and, it is demonstrated to be suitable in the Cartesian coordinate fix grid system used here. The KBC method is proven to be convenient for moderate non-breaking waves, and it is easy to implement, computationally efficient, and requires minimum memory storage. Many moderate non-breaking wave simulating models have used KBC to determine the position of the free surface in the existing CFD method such as finite difference method (FDM) and finite volume method (FVM).

In this paper, a new method based on the combination of LBE and KBC for modeling the two-dimensional (2D) viscous free surface wave is proposed. With an attempt to establish the LBE–KBC method, three major works are constructed. First, the LBE equilibrium distribution

functions are modified so that only the non-hydrostatic pressure is included. The hydrostatic part, which is expressed as a function of free surface elevation, is added as a force term to the LBE with a finite difference scheme. The purpose of dividing the total pressure into the hydrostatic part and non-hydrostatic part is to exactly express the force caused by the hydrostatic part at the free surface. Second, the LBE free surface boundary condition (FSBC) is improved from previous study [28] with higher accuracy. And third, interpolation-supplemented lattice Boltzmann (ISLB) method [43, 44] is introduced to simulate waves on arbitrary and nonuniform meshes, which much enhance the flexibility and the computational efficiency of the LBE–KBC method. In order to validate the proposed LBE–KBC method, five different cases of stationary flow, solitary wave, standing waves, small amplitude Stokes wave and waves traveling over a submerged bar are simulated, respectively. In addition, the computational performance of the LBE–KBC scheme is investigated.

2. NUMERICAL METHODS

2.1. Governing equations

The 2D incompressible viscous flow is governed by the continuity equation and the Navier–Stokes equations,

$$\frac{\partial u}{\partial x} + \frac{\partial v}{\partial y} = 0, \quad (1)$$

$$\frac{\partial u}{\partial t} + u \frac{\partial u}{\partial x} + v \frac{\partial u}{\partial y} = -\frac{1}{\rho_0} \frac{\partial p}{\partial x} + \nu \left(\frac{\partial^2 u}{\partial x^2} + \frac{\partial^2 u}{\partial y^2} \right), \quad (2)$$

$$\frac{\partial v}{\partial t} + u \frac{\partial v}{\partial x} + v \frac{\partial v}{\partial y} = -\frac{1}{\rho_0} \frac{\partial p}{\partial y} + \nu \left(\frac{\partial^2 v}{\partial x^2} + \frac{\partial^2 v}{\partial y^2} \right) - g, \quad (3)$$

where u and v are the fluid velocities in the x and y directions, respectively, ρ_0 and ν are the constant density and kinematic viscosity of the fluid, p denotes the total pressure and g is the gravitational acceleration. The total pressure p can be further divided into two components:

$$p = p_H + p_D, \quad (4)$$

where p_H and p_D are hydrostatic pressure and non-hydrostatic pressure, respectively. The hydrostatic pressure is defined as

$$p_H = \rho_0 g (\eta - y), \quad (5)$$

where $\eta(x, t)$ is the free surface elevation (see Figure 1). Inserting Equations (4) ~ (5) into Equations (2) ~ (3), we have

$$\frac{\partial u}{\partial t} + u \frac{\partial u}{\partial x} + v \frac{\partial u}{\partial y} = -g \frac{\partial \eta}{\partial x} - \frac{1}{\rho_0} \frac{\partial p_D}{\partial x} + \nu \left(\frac{\partial^2 u}{\partial x^2} + \frac{\partial^2 u}{\partial y^2} \right), \quad (6)$$

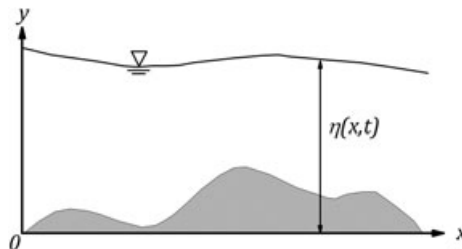


Figure 1. Definition of free surface elevation.

$$\frac{\partial v}{\partial t} + u \frac{\partial v}{\partial x} + v \frac{\partial v}{\partial y} = -\frac{1}{\rho_0} \frac{\partial p_D}{\partial y} + v \left(\frac{\partial^2 v}{\partial x^2} + \frac{\partial^2 v}{\partial y^2} \right), \quad (7)$$

where η and p_D become the unknown variable instead of p . Here, η is a single-valued height function, which has been proven to be well suited for small or moderate non-breaking waves [16, 17, 34]. The KBC can be written in a Eulerian form obtained through a Taylor series expansion [45]

$$\frac{\partial \eta}{\partial t} + u_s \frac{\partial \eta}{\partial x} = v_s, \quad (8)$$

where u_s and v_s are horizontal and vertical velocities on the free surface, respectively. The outlet boundary is a rigid wall with an artificial damping layer on the free surface to absorb the wave energy. Then the KBC of Equation (8) is modified by a damping term as [13]

$$\frac{\partial \eta}{\partial t} + u_s \frac{\partial \eta}{\partial x} = v_s - \gamma(x)(\eta - \eta_0), \quad (9)$$

where $\gamma(x)$ is the damping coefficient, and η_0 is a reference value specifying the at-rest position of a fluid particle. $\gamma(x)$ can be defined as

$$\gamma(x) = \begin{cases} \omega \left(\frac{x-x_0}{\lambda} \right)^2, & x \geq x_0 = L_D - \lambda, \\ 0, & x < x_0, \end{cases} \quad (10)$$

where λ and ω are the representative wave wavelength and wave frequency, respectively, and L_D is the position of the far field boundary.

2.2. The lattice Boltzmann equation–kinematic boundary condition method

A new method is proposed to solve the 2D free surface wave model described in the previous section. The general features of our method are: (1) The LBE method is applied to solve the interior flow field. The multi-relaxation-time (MRT) model is used to enhance the stability of the proposed method. Furthermore, the ISLB method is established to enable our method to be applied on arbitrary, nonuniform mesh grids. (2) The KBC, which is explicitly discretized using FDM, is solved to obtain the free surface elevation with every grid cell being marked as ‘filled’, ‘empty’ or ‘interface’ to depict the state of the cell. (3) The FSBC for LBE is revised to enable our method to be applied in the coarse grid systems while keeping the accuracy of the results. The details of the proposed method are fully described succeedingly.

2.2.1. Lattice Boltzmann equation for flow field. The LBE is introduced to solve the governing equations. In the present 2D model, space is discretized into a square lattice, and there are nine discrete velocities given by (Figure 2)

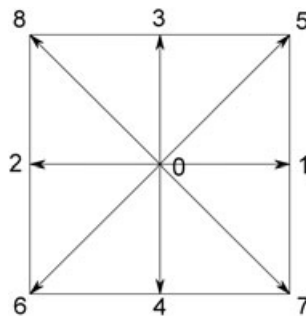


Figure 2. Discrete lattice and the trajectory of particles.

$$\mathbf{e}_a = \begin{cases} \mathbf{0}, & a = 0, \\ \cos\left[\frac{(a-1)\pi}{2}\right] e\mathbf{i} + \sin\left[\frac{(a-1)\pi}{2}\right] e\mathbf{j}, & a = 1-4, \\ \cos\left[\frac{(a-1)\pi}{2} + \frac{\pi}{4}\right] \sqrt{2}e\mathbf{i} + \sin\left[\frac{(a-1)\pi}{2} + \frac{\pi}{4}\right] \sqrt{2}e\mathbf{j}, & a = 5-8. \end{cases} \quad (11)$$

where $e = \delta x / \delta t$ is the particle velocity, and δx and δt are the lattice grid spacing and time step, respectively.

The lattice Boltzmann method consists of two steps: a collision step and a streaming step. The LBE with nine-speed lattice can be written as

$$\text{Collision and forcing } f'_a(\mathbf{x}, t) = f_a(\mathbf{x}, t) + \Omega_a + \delta t F_a, \quad (12)$$

$$\text{Streaming } f_a(\mathbf{x} + \mathbf{e}_a \delta t, t + \delta t) = f'_a(\mathbf{x}, t), a = 0-8, \quad (13)$$

where f_a is the distribution function of particles and f'_a represents the post-collision state; F_a is related to the force term; Ω_a must satisfy conservation laws and be compatible with the symmetry of the model approximated by single-relaxation-time lattice Bhatnagar–Gross–Krook (BGK) model:

$$\Omega_a = -\frac{1}{\tau} (f_a(\mathbf{x}, t) - f_a^{\text{eq}}(\mathbf{x}, t)) \quad (14)$$

where τ is the dimensionless relaxation time and f_a^{eq} is the equilibrium distribution function. f_a^{eq} can be defined as

$$f_a^{\text{eq}} = \begin{cases} \rho_0 - (1 - \omega_0) \frac{pD/\rho_0}{c_s^2} + s_0(\mathbf{u}), & a = 0, \\ \omega_a \frac{pD/\rho_0}{c_s^2} + s_a(\mathbf{u}), & a = 1-8, \end{cases} \quad (15)$$

where $s_a(\mathbf{u}) = \omega_a [3\mathbf{e}_a \cdot \mathbf{u}/e^2 + 4.5(\mathbf{e}_a \cdot \mathbf{u}/e^2)^2 - 1.5|\mathbf{u}|^2/e^2]$; ω_a is the weight coefficient: $\omega_0 = 4/9$, $\omega_{1-4} = 1/9$, $\omega_{5-8} = 1/36$; $c_s = e/\sqrt{3}$ is the speed of sound; It is worth noticing that f_a^{eq} includes only the non-hydrostatic pressure whereas the hydrostatic part $-g \frac{\partial \eta}{\partial x}$ is contained in the force term F_a . The hydrostatic part, which is related to the gravity and the gradient of the free surface elevation, can be easily and correctly expressed in every filled cell or interface cell. Unlike the VOF-like LB method [28], the gravity here is not weighted by the fluid fraction of the cell, but it is contained in the hydrostatic part. It reduces the errors caused by the fluid fraction. Thus Equations (1) and (6)~(7) can be correctly recovered.

Accordingly, the MRT LBE reads

$$\Omega_a = -\mathbf{S}(\hat{f}_a - \hat{f}_a^{\text{eq}}), \quad (16)$$

where \hat{f}_a^{eq} is the equilibrium value of the moment \hat{f}_a ; \mathbf{S} is collision matrix. The nine eigenvalues of \mathbf{S} are all between 0 and 2 so as to maintain linear stability and the separation of scales. The evolutionary equation of the MRT LBE becomes

$$\text{Collision and Forcing } f'_a(\mathbf{x}, t) = f_a(\mathbf{x}, t) - \mathbf{M}^{-1} \hat{\mathbf{S}}(\hat{f}_a - \hat{f}_a^{\text{eq}}) + \delta t F_a, \quad (17)$$

$$\text{Streaming } f_a(\mathbf{x} + \mathbf{e}_a \delta t, t + \delta t) = f'_a(\mathbf{x}, t), a = 0-8, \quad (18)$$

where $\hat{\mathbf{f}} = \mathbf{M}\mathbf{f}$, $\mathbf{f} = \mathbf{M}^{-1}\hat{\mathbf{f}}$ and the bold-face symbols denote nine-dimensional column vectors, for example, $\mathbf{f} = [f_0, f_1, \dots, f_8]^T$. The collision matrix $\hat{\mathbf{S}} = \mathbf{M}\mathbf{S}\mathbf{M}^{-1}$ in moment space is a diagonal matrix given by

$$\hat{\mathbf{S}} = \text{diag}[s_1, s_2, s_3, s_4, s_5, s_6, s_7, s_8, s_9]. \quad (19)$$

Following the method of Ginzburg, the transformation matrix \mathbf{M} of the incompressible MRT LBE and the corresponding equilibrium distribution functions in moment space \hat{f}_a^{eq} are listed in Table I.

Table I. The transformation matrix.

\mathbf{e}_k	$\mathbf{f}^{\text{eq}} \cdot \mathbf{e}_k$									
p	1	1	1	1	1	1	1	1	1	ρ_0
e	-4	-1	-1	-1	-1	2	2	2	2	$6(p_D/\rho_0)/e^2 + 3(u_x^2 + u_y^2)/e^2 - 4\rho_0$
e^2	4	-2	-2	-2	-2	1	1	1	1	$-9(p_D/\rho_0)/e^2 - 3(u_x^2 + u_y^2)/e^2 + 4\rho_0$
u_x	0	1	-1	0	0	1	-1	1	-1	u_x/e
q_x	0	-2	2	0	0	1	-1	1	-1	$-u_x/e$
u_y	0	0	0	1	-1	1	-1	-1	1	u_y/e
q_y	0	0	0	-2	2	1	-1	-1	1	$-u_y/e$
p_{xx}	0	1	1	-1	-1	0	0	0	0	$(u_x^2 - u_y^2)/e^2$
p_{xy}	0	0	0	0	0	1	1	-1	-1	$u_x u_y / e^2$

For the forcing term F_a , the Guo–Zheng–Shi model [46] is used for higher accuracy and has the following MRT form:

$$\mathbf{F} = \mathbf{M}^{-1} \left(\mathbf{I} - \frac{1}{2} \mathbf{S} \right) \mathbf{M} \bar{\mathbf{F}}, \quad (20)$$

where $\mathbf{F} = (F_1, F_2, \dots, F_a)^T$, $\bar{\mathbf{F}} = (\bar{F}_1, \bar{F}_2, \dots, \bar{F}_a)^T$, and

$$\bar{F}_a = \omega_a \left[\frac{\mathbf{e}_a \cdot \mathbf{F} \mathbf{c}}{c_s^2} + \frac{\mathbf{u} \mathbf{F} \mathbf{c} : (\mathbf{e}_a \mathbf{e}_a - c_s^2 \mathbf{I})}{c_s^4} \right]. \quad (21)$$

Here, $\mathbf{F} \mathbf{c} = (-g \frac{\partial \eta}{\partial x}, 0)$ is the force. According to the Guo–Zheng–Shi model, the definition of the velocity is modified. So, the velocity \mathbf{u} and the non-hydrostatic pressure p_D are defined in terms of the distribution function as

$$\mathbf{u} = \sum_{a=1}^8 \mathbf{e}_a f_a + \frac{\delta t}{2} \mathbf{F} \mathbf{c}, \quad (22)$$

$$p_D = \frac{c_s^2 \rho_0}{1 - \omega_0} \left[\sum_{a=1}^8 f_a + s_0(\mathbf{u}) \right], \quad (23)$$

The free surface elevation η cannot be obtained directly from the distribution function, and it will be discussed in Section 2.2.2.

Through the Chapman Engskog procedure, the Equations (1) and (6)~(7) can be recovered, and the viscosity is

$$\nu = \frac{\delta t}{6} (2\tau - 1) e^2 \quad (24)$$

and $s_8 = s_9 = 1/\tau$. The relaxation parameters in the collision matrix $\hat{\mathbf{S}}$ are chosen to be $s_1 = s_4 = s_6 = 1.0$, $s_8 = s_9 = 1/\tau$, $s_5 = s_7 = 1.2$, $s_2 = s_5 - 0.1$, $s_3 = s_2 - 0.1$ according to [47].

The proposed method is based alternatively on arbitrary and nonuniform mesh grids. In order to expand LBE to nonuniform mesh, the ISLB method [43, 44] is implemented. The evolution of the LBE on a nonuniform mesh consists of three steps: collision, streaming, and interpolation. The initial values of f_a are specified at each grid point (X_i, Y_j) . The second-order central difference interpolation is used in the interior of the flow field, and the second-order upwind interpolation is applied to the mesh grids next to boundaries. Considering a nonuniform rectangular computational mesh, let (X_i, Y_j) denote a grid point on an arbitrary rectangular computational mesh in a Cartesian coordinate system. We have

$$\mathrm{d}X_i = (X_{i+1} - X_{i-1})/2, \quad (25)$$

$$dY_j = (Y_{j+1} - Y_{j-1})/2, \quad (26)$$

where dX_i and dY_j denote grid sizes. The ratio of nonuniform to uniform grid sizes can be defined as

$$r_x^i = dX_i/\delta x, \quad (27)$$

$$r_y^j = dY_j/\delta y. \quad (28)$$

For the nine-speed LBE in 2D space, the mesh is a uniform square lattice grid with $\delta x = \delta y$.

2.2.2. Free surface tracking. A free surface represents a moving boundary from a numerical point of view. To track the free surface, the fluid fraction ϵ needs to be stored for each cell. A fill level of $\epsilon = 0$ indicates a completely empty cell (E-cell); whereas a fill level of $\epsilon = 1$ indicates a completely filled cell (F-cell); a fill level of $0 < \epsilon < 1$ indicates an interface cell (I-cell). However, in order to maintain the interface cells closed, there may be some interface cells, which have the fill level equals to zero, see Figure 3.

In this work, the movement of the fluid interface is tracked by the free surface elevation η . As η cannot be obtained directly from the distribution functions of LBE, a finite different method is used to discretize Equation (8) in order to obtain the value of η based on the results of $\mathbf{u}_s = (u_s, v_s)$ obtained from LBE. Discretized form of Equation (8) can be written as

$$\eta_P^{n+1} = \left[v_{s,P}^n - \frac{u_{s,P}^n (\eta_e^n - \eta_w^n)}{dX} \right] \cdot \delta t + \eta_P^n, \quad (29)$$

where η_e^n and η_w^n are the east and west free surface elevations and are obtained by the second order upwind interpolation scheme, respectively.

The velocity \mathbf{u}_s at the free surface can be obtained from the fluid domain using a three-point formula interpolation or extrapolation [16]:

$$u_s = Au_{i,j} + Bu_{i,j-1} + Cu_{i,j-2}, \quad (30)$$

$$v_s = Av_{i,j} + Bv_{i,j-1} + Cv_{i,j-2}, \quad (31)$$

$$A = \left(r_y^j \cdot \epsilon_{i,j} + \frac{r_y^{j-1}}{2} \right) \cdot \left(r_y^j \cdot \epsilon_{i,j} + r_y^{j-1} + \frac{r_y^{j-2}}{2} \right) / \left(\frac{r_y^j + r_y^{j-1}}{2} \right) / \left(\frac{r_y^j + r_y^{j-2}}{2} + r_y^{j-1} \right), \quad (32)$$

$$B = r_y^j \cdot (\epsilon_{i,j} - 0.5) \cdot \left(r_y^j \cdot \epsilon_{i,j} + r_y^{j-1} + \frac{r_y^{j-2}}{2} \right) / \left(-\frac{r_y^j + r_y^{j-1}}{2} \right) / \left(\frac{r_y^{j-1} + r_y^{j-2}}{2} \right), \quad (33)$$

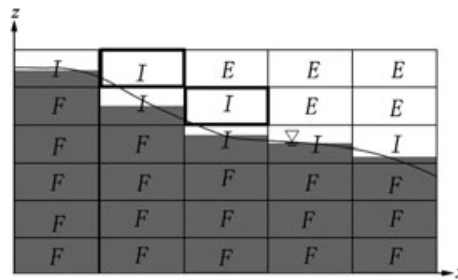


Figure 3. Definition of interface cells. The interface cells that are highlighted by the black frames have the filled levels $\epsilon = 0$.

$$C = r_y^j \cdot (\epsilon_{i,j} - 0.5) \cdot \left(r_y^j \cdot \epsilon_{i,j} + \frac{r_y^{j-1}}{2} \right) / \left(\frac{r_y^j + r_y^{j-2}}{2} + r_y^{j-1} \right) / \left(\frac{r_y^{j-1} + r_y^{j-2}}{2} \right), \quad (34)$$

where (i, j) denotes the position of the I-cell that contains the free surface.

After the free surface elevation is calculated, the states of the cells need to be changed correspondingly. The cells below, located at and above the free surface elevation are respectively converted to F-cells, I-cells and E-cells. During these changes, ϵ is recalculated accordingly. If the E-cells are converted to F-cells for each of these, the average velocity \mathbf{v}^{avg} and the average non-hydrostatic pressure p_D^{avg} of surrounding fluid and interface cells is computed; if the E-cells are converted to I-cells, p_D^{avg} is calculated by a three-point formula interpolation or extrapolation, and the free surface boundary pressure $p_D^{\text{surface}} = 0$ is used. The distribution function of the E-cells are initialized with the equilibrium function $f_a^{\text{eq}}(p_D^{\text{avg}}, \mathbf{v}^{\text{avg}})$ [27].

After the step described earlier, a problem may occur: the I-cells are not closed. So, an extra step is needed: if an F-cell has an empty neighboring cell, the empty neighboring cell is converted to I-cell. \mathbf{v}_{avg} , p_D^{avg} and $f_a^{\text{eq}}(p_D^{\text{avg}}, \mathbf{v}^{\text{avg}})$ are obtained from the surrounding fluid and I-cells. However, ϵ remains zero for maintaining the mass conservation.

2.2.3. Boundary conditions. In this paper, the modified bounce-back scheme [48] of no-slip boundary conditions is used to treat the rough boundaries. Meanwhile, the modified specular reflection scheme [49] is used to treat the slip boundaries. At the inflow and outflow boundaries, the non-equilibrium extrapolation method [50] is used. All of these boundary schemes are of second-order accuracy.

In our investigations, we found that different free surface boundary conditions may improve the numerical results significantly. Hence, the free surface boundary needs to be treated carefully. Here, a scheme that enforces the equality in fluid pressure and surrounding pressure is used [28]:

$$f'_I(\mathbf{x} - \mathbf{e}_i, t) = -f'_i(\mathbf{x}, t) + f_I^{\text{eq}}(p_D(\mathbf{x}, t), \mathbf{u}(\mathbf{x}, t)) + f_i^{\text{eq}}(p_D(\mathbf{x}, t), \mathbf{u}(\mathbf{x}, t)), \quad (35)$$

where $f'_I(\mathbf{x} - \mathbf{e}_i, t)$ and $f'_i(\mathbf{x}, t)$ are anti-parallel incoming and outgoing distribution functions, respectively; $f_I^{\text{eq}}(p_D(\mathbf{x}, t), \mathbf{u}(\mathbf{x}, t))$ are the equilibrium distribution functions; $p_D(\mathbf{x}, t)$ and $\mathbf{u}(\mathbf{x}, t)$ are related to the surrounding non-hydrostatic pressure and velocities, respectively; for incompressible fluids such as water, it is sufficiently accurate to use condition $p_D = 0$ along the free surface [35]. Then, $p_D(\mathbf{x}, t)$ is calculated by the three-point formula interpolation or extrapolation.

Then, all distribution functions at the free surface with $\mathbf{e}_i \cdot \mathbf{n} \geq 0$ and the missing distribution functions are reconstructed using Equation (35), where $\mathbf{n} = (n_1, n_2)$ is the normal vector to the free surface and can be calculated as [17]

$$n_1 = \frac{-\partial\eta/\partial x}{\sqrt{(\partial\eta/\partial x)^2 + 1}}, \quad (36)$$

$$n_2 = \frac{1}{\sqrt{(\partial\eta/\partial x)^2 + 1}}. \quad (37)$$

The centered difference scheme is adopted to discretize Equations (36)~(37). Hence, the normal vector is second-order accurate in space. The ‘reconstructed condition’ is successfully applied to the model proposed by Körner *et al.* [28] for foaming simulation. However, it is found that this ‘reconstructed condition’ cannot accurately model the water wave propagation and even leads to the simulation collapse in a coarse grid system. In the study of Körner, the distribution functions coming from the neighboring I-cells with $\mathbf{e}_i \cdot \mathbf{n} \geq 0$ are reconstructed. It means that these neighboring I-cells are treated as E-cells, and the information coming from these neighboring I-cells are not considered. For this contradiction, Körner supposes the I-cells could be treated as E-cells or F-cells depending on the interface orientation. According to our study, we found that the hypothesis might not be the best choice. We inclined to treat the I-cells with $|\mathbf{e}_i \cdot \mathbf{n}| \approx 0$ as F-cells, and the distribution functions coming from the neighboring I-cells with $|\mathbf{e}_i \cdot \mathbf{n}| \approx 0$ should not be reconstructed. Although, the pressure at the free surface may not be exactly satisfied, the information

coming from the neighboring I-cells are fully taken into account (See Appendix A for detail). To decide which distribution functions should be reconstructed, here, we introduce the standard normal vectors, which are defined as follows: $\mathbf{n}_s = (-1,0), (-1,-1), (0,-1), (1,-1), (1,0)$. Five types of the reconstructed conditions are defined according to the value of $\partial\eta/\partial x$ (Table II). The obtainment of the five types is given in detail in Appendix A consequently. The reconstructed condition is revised as $\mathbf{e}_i \cdot \mathbf{n}_s > 0$ with the purpose of excluding the distribution functions coming from the neighboring I-cells with $|\mathbf{e}_i \cdot \mathbf{n}| \approx 0$. However, it is worth noticing that the distribution functions coming from the neighboring I-cells with $|\mathbf{e}_i \cdot \mathbf{n}| \gg 0$ should be reconstructed. To investigate the present revised-FSBC and the former-FSBC, the numerical experiments are investigated in the subsequent section.

2.2.4. The computational procedure. As a brief summary, the computational procedure of our LBE–KBC method is as follows:

Algorithm 1 The main calculation loop

- 1: Input mesh information and initial values of all variables
 - 2: Input the total simulated time step tn
 - 3: **for** $n = 0$ to tn **do**
 - 4: Collision and forcing (Eq.(17))
 - 5: Apply boundary conditions: FSBC and other boundary conditions (Section 2.2.3)
 - 6: Steaming and the $f_a(\mathbf{x} + \mathbf{e}_a\delta t, t + \delta t)$ are obtained (Eq.(18))
 - 7: Compute $f_a(\{\mathbf{x}\}, t + \delta t)$ from $f_a(\{\mathbf{x} + \mathbf{e}_a\delta t\}, t + \delta t)$ by interpolation (ISLB method)
 - 8: Calculate \mathbf{u} and p_D (Eqs. (22)~(23))
 - 9: Calculate η^{n+1} using \mathbf{u}_s obtained from \mathbf{u} using Eqs.(30)~(34) (Eq.(29))
 - 10: Change the states of the cells according to the free surface elevation η^{n+1}
 - 11: **end for**
-

3. NUMERICAL ANALYSIS

In this section, the incompressible fluid dynamics are simulated and the Mach number (Ma) ≤ 0.3 must be guaranteed [51]. Ma can be defined as $\sqrt{3}u^*/e$, where u^* is the characteristic velocity. Five different cases are considered to validate the LBE–KBC method. The first three cases concern stationary flow, solitary wave and standing waves with viscous effects. The fourth and fifth cases simulate wave propagation in a tank and extend the model to consider the deformation of waves traveling over a submerged bar, respectively. The numerical results are compared with analytical solutions and/or experimental data.

3.1. Stationary flow

The first case is a stationary flow in a rectangular tank of length 1 m and depth 3 m, which is designed to investigate the accuracy of the FSBCs under different fluid fractions of I-cells and different inclinations of free surface. Free-slip boundary conditions are used for the sides and bottom.

Table II. Five types of the reconstructed conditions.

$\partial\eta/\partial x$	\mathbf{n}_s	Directions not to be reconstructed
$(-\infty, -2]$	$(-1,0)$	3,4
$(-2, -0.5]$	$(-1,-1)$	7,8
$(-0.5, 0.5]$	$(0,-1)$	1,2
$(0.5, 2]$	$(1,-1)$	5,6
$(2, +\infty)$	$(1,0)$	3,4

To keep the flow stationary under a specific inclination of free surface, the force is specified as

$$\mathbf{F}_c = \left(-g \frac{\partial \eta}{\partial x} - g L_{\text{Inc}}, 0 \right), \quad (38)$$

where L_{Inc} is the inclination of the initial free surface. In the computation, $dX = dY = \delta x = \delta y = 0.03125$ m and $e = 20$ m/s, the LB viscosity $\tau = 0.5531$ (the kinematic viscosity $\nu = 0.01108$ m²/s). First, a numerical experimentation is designed to investigate the effect of fluid fraction ϵ of the I-cells on the accuracy of the results. Here $L_{\text{Inc}} = 0$, $\epsilon = 0 \sim 1$ and the still free surface elevation is set to $\eta = 1 - (0.5 - \epsilon)\delta x$ m, respectively. For example, when $\epsilon = 0.5$, $\eta = 1$ m, it can be found that every I-cell has the fluid fraction $\epsilon = 0.5$. The velocities of m I-cells are compared with the exact solutions of $u_{\text{exa}} = 0$ and $v_{\text{exa}} = 0$,

$$\text{Error} = \frac{\sum_{i=1}^m \sqrt{(u_i - u_{\text{exa}})^2 + (v_i - v_{\text{exa}})^2}}{m} \quad (39)$$

It is found that more accurate results are obtained by the revised-FSBC than the former-FSBC under different values of ϵ (Figure 4).

Moreover, free surfaces with different inclinations are simulated. The initial free surface elevation is set to $\eta = 2 + L_{\text{Inc}}(x - 0.5)$ m, where $L_{\text{Inc}} = 0 \sim 2$. As it is shown in Figure 5, errors of the LBE-KBC with revised-FSBC are smaller near the regions of $L_{\text{Inc}} = 0$ and 1, which is due to the reason that the pressure near the free surface is exactly satisfied and the momentum fluxes between the I-cells are completely fulfilled in these regions. It can also be seen that although the pressure near the free surface is satisfied, the errors of the scheme with the former-FSBC are larger than that of the revised-FSBC, which fully considers the momentum fluxes between the I-cells.

3.2. Solitary wave test

The solitary wave is a finite amplitude wave that consists of a single displacement of water above the mean water level. Many non-hydrostatic models have been applied to simulate this wave problem to verify their models' accuracy [16, 17, 33, 35].

In this test, the wave amplitude $a = 3$ m and the mean water depth $h = 15$ m. The computational domain is from 0 to 800 m. At the inflow boundary ($x = 0$ m), the velocity is prescribed in terms of solitary wave theory and at the outflow boundary ($x = 800$ m), a radiation condition is imposed to minimize wave reflection. The analytical solution of the free surface elevation is

$$\eta(x, t) = 4a \frac{\exp[-2\Phi(x - ct)]}{\{1 + \exp[-2\Phi(x - ct)]\}^2} + h, \quad (40)$$

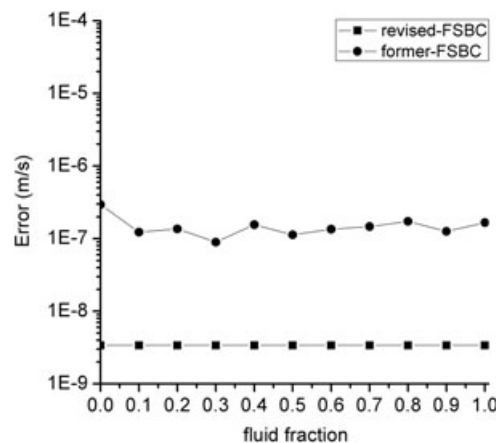


Figure 4. Comparison of errors of lattice Boltzmann equation–kinematic boundary condition using the revised-free surface boundary condition (revised-FSBC) and the former-FSBC under different fluid fractions (simulation time step $tn=2800$).

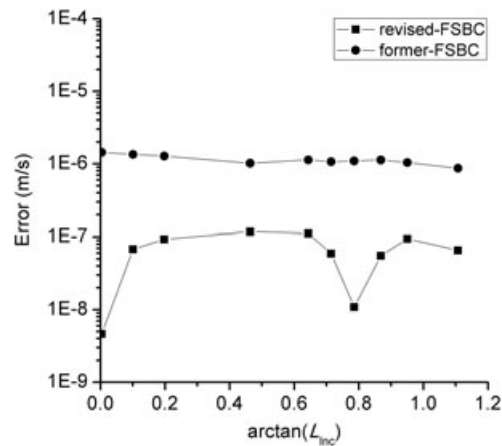


Figure 5. Comparison of errors of lattice Boltzmann equation–kinematic boundary condition using the revised-FSBC and the former-FSBC under different inclinations of free surface (simulation time step $tn=2800$).

$$c = \sqrt{g(h+a)}, \quad \Phi = \frac{1}{2h} \sqrt{\frac{3a}{h+a}}. \quad (41)$$

In this section, solitary wave problem is simulated to specially investigate the efficiency of our revised-FSBC, which is used in the remaining cases in this paper. Nine scenarios (Table III) are designed to investigate the grid convergences of the scheme with the former-FSBC and the revised-FSBC. In these sections, for all the calculations, the kinematic viscosity is taken as $\nu = 1.14 \times 10^{-6} \text{ m}^2/\text{s}$, $\text{Ma} < 0.07$ ($u^* = \sqrt{gh \frac{a}{h}}$), $\text{Re} = \frac{u^* h}{\nu} = 3.19 \times 10^6$ and $\text{Fr} = u^* / \sqrt{gh} = 0.2$. Scenarios of group 1 are designed to investigate the grid convergences of the model without the ISLB method and scenarios of groups 2 and 3 are used to test the grid convergences with the ISLB method in the vertical and horizontal directions, respectively.

Figure 6 shows the wave high differences of group 1 at $t = 40 \text{ s}$ simulated by the former-FSBC and the revised-FSBC. The convergence orders of the scheme using the former-FSBC and the revised-FSBC are about 2.5 and 2.1, respectively. However, more accurate results are obtained by the revised-FSBC. It indicates that a nearly convergent solution can be obtained using a grid spacing $\delta x = 4 \text{ m}$. Figures 7 and 8 indicate that the results of groups 2 and 3 using the revised-FSBC have better grid convergence and accuracy. Moreover, it can also be observed that the convergence order is more sensitive to the horizontal direction than the vertical direction. Comparison of wave high differences between group 1 (without ISLB) and group 3 (with ISLB) is illustrated in Figure 9, from which we can see that the accuracy of the results are very closed to each other. However, less cells in the vertical direction is needed in group 1. Overall, the scheme using the revised-FSBC has better grid convergence and accuracy with or without the ISLB method.

Table III. Simulation scenarios.

Group	Scenario	$\delta x, \delta y \text{ (m)}$	$e \text{ (m/s)}$	$dX \text{ (m)}$	$dY \text{ (m)}$
1	1	2	120	2	2
	2	4	240	4	4
	3	8	480	8	8
	4	1	60	4	1
2	5	1	60	4	2
	6	1	60	4	3
	7	1	60	4	4
	8	1	60	2	1
3	4	1	60	4	1
	9	1	60	8	1

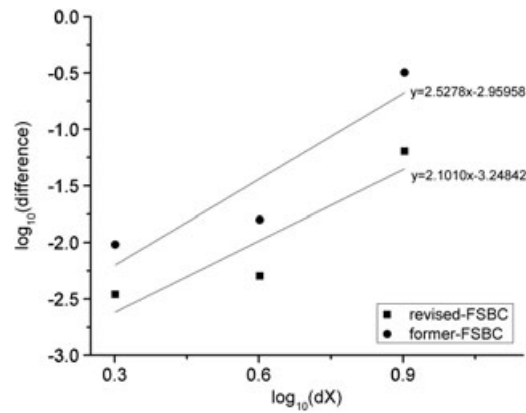


Figure 6. Comparison of the wave high differences of group 1 simulated by the former-FSBC and the revised-FSBC. The convergence orders of the simulated results by the former-FSBC and revised-FSBC are 2.5 and 2.1, respectively.

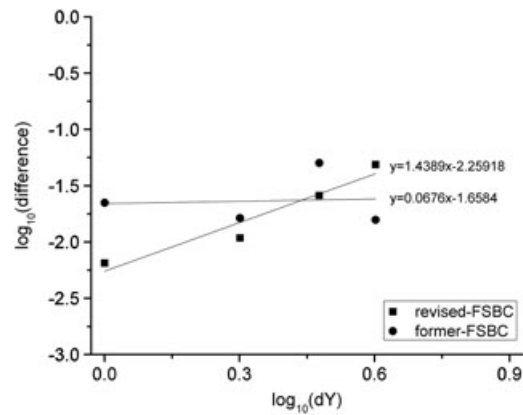


Figure 7. Comparison of the wave high differences of group 2 simulated by the former-FSBC and the revised-FSBC. The convergence orders of the simulated results by the former-FSBC and revised-FSBC are 0.1 and 1.4, respectively.

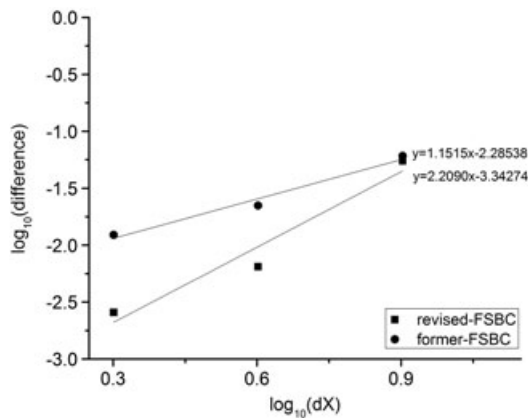


Figure 8. Comparison of the wave high differences of group 3 simulated by the former-FSBC and the revised-FSBC. The convergence orders of the simulated results by the former-FSBC and revised-FSBC are 1.2 and 2.2, respectively.

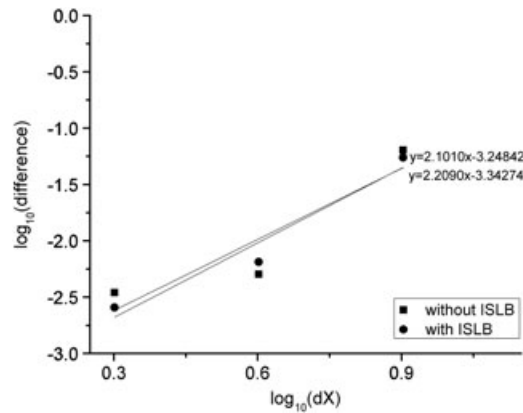


Figure 9. Comparison of the wave high differences between groups 1 and 3 simulated by the revised-FSBC. The convergence orders of the simulated results of groups 1 and 3 are 2.1 and 2.2, respectively.

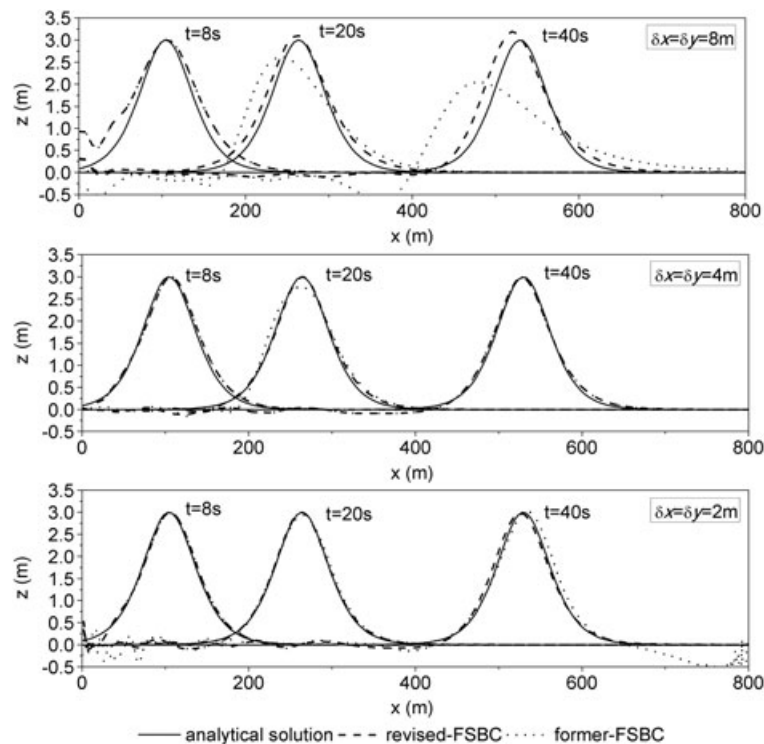


Figure 10. Comparison of free surface elevation obtained by revised-FSBC and former-FSBC with analytical solution at three different times ($t=8, 20$ and 40 s) for group 1.

In Figure 10, the numerical results of the free surface elevation obtained by revised-FSBC and former-FSBC are compared with the analytical solution at three different times ($t = 8, 20$ and 40 s) for group 1. Results show that the wave shapes can be well kept at different times by revised-FSBC even using a very coarse grid system.

3.3. Standing waves with viscous effects

The case of standing waves in a rectangular basin of length 1 m and depth $d = 1$ m, designed by previous research [15], is performed. Free-slip boundary conditions are used for the sides and bottom. The wave length $l = 2$ m, the wave period $T = 1.1339$ s and the wave number $k = 3.1$.

Simulations are run for small amplitude waves with a wave height of 0.02 m and for finite amplitude waves with a wave height of 0.2 m. Parameters of the five scenarios are listed in Table IV. For all the five scenarios, $Ma \leq 0.3$, and it can be seen as the incompressible fluid [51]. The damping of the wave amplitude because of viscosity as a function of time is approximated from [52]:

$$a(t) = a(0)e^{-2\nu k^2 t}, \quad (42)$$

The linear analytical solution and the nonlinear analytical solution can be written as

$$\eta(x, t) = a(t) \cos(kx - \omega t) + d, \quad (43)$$

$$\eta(x, t) = a(t) \cos(kx - \omega t) + \frac{\pi a(t)^2}{2l} \left(1 + \frac{3}{2 \sinh^2 kd} \right) \coth(kd) \cos(2kx - 2\omega t) + d, \quad (44)$$

To investigate grid convergence, four different meshes, denoted by Mesh 1, Mesh 2, Mesh 3, Mesh 4, using 8×12 , 16×20 , 24×28 , 32×38 cells are respectively adopted in scenario 4. Here $dX = dY = \delta x = \delta y$ for all cells, and there is thus no interpolation step during the calculation. In Figure 11, results for the position of the free surface at the left boundary against time are compared with the nonlinear analytical solution, from which we can observe that the numerical results with different meshes approach the nonlinear analytical solution gradually. We also investigate grid convergence with the grids clustering near surface layers. Simulations are performed using 19, 25 and 37 layers along the water depth, and the center layer thickness is $dY = 4\delta y$, $2\delta y$ and δy , respectively; the uniform horizontal grid size is $dX = \delta x$, and there are 32 cells in the horizontal direction (see Figure 12). The ISLB method is adopted. Figure 13 shows that the numerical results with different layer thicknesses are perfectly closed to the nonlinear analytical solution. Figure 14 shows the differences of the period, wave height and nonlinear wave shape between the simulating results and the theory solution on different meshes for four periods, from which we find that the convergence order of period is about second-order accurate, and the convergence order of wave height and the nonlinear wave shape are between first-order and second-order accurate.

Furthermore, we use the mesh of 32×25 for all scenarios in this section. The particle velocity $e = 20$ m/s, and therefore the time interval $\delta t \approx 0.00138 T$.

Table IV. Simulation scenarios.

Scenario	a (m)	Re	LB viscosity	Ma	Fr
1	0.01	10	0.5531	0.0048	0.013
2	0.01	100	0.5053	0.0048	0.013
3	0.1	10	1.0310	0.0480	0.130
4	0.1	100	0.5531	0.0480	0.130
5	0.1	1000	0.5053	0.0480	0.130

a , wave amplitude; Re, Reynolds number ($=La\omega/\nu$), ω is the wave frequency and ν is the kinematical viscosity; Ma, Mach number ($=\sqrt{3}a\omega/e$); Fr, Froude number ($=a\omega/\sqrt{gL}$).

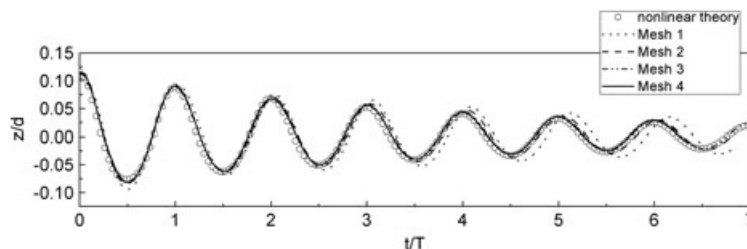


Figure 11. Convergence of free surface elevation on the left side wall with different meshes.

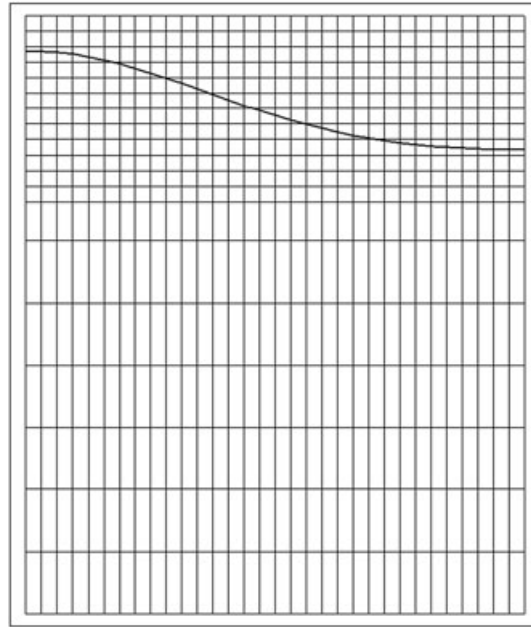


Figure 12. The computational mesh of 32×19 with the nonlinear initial wave shape.

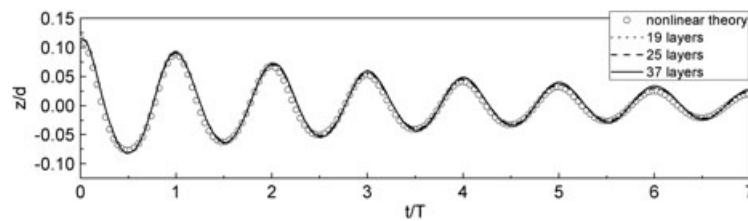


Figure 13. Convergence of free surface elevation on the left side wall with different vertical layers.

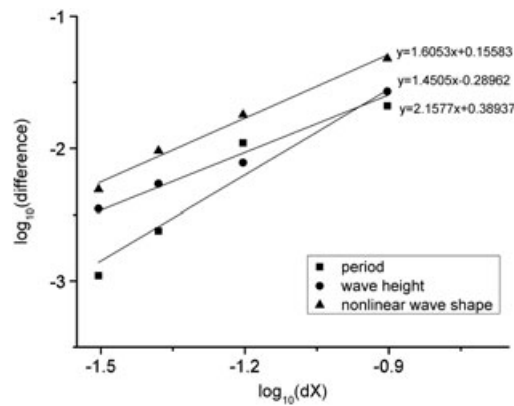


Figure 14. The period, wave height and nonlinear wave shape differences between the simulating results and the theory solutions on different meshes for the four periods. The convergence orders of the period, wave height and nonlinear wave shape are 2.2, 1.5 and 1.6, respectively.

For comparison, the numerical results of the 2D finite-volume scheme developed by Hodges *et al.* [15] are included. In Table V, comparisons of the simulated results with the analytical solutions are listed for each scenario. It is seen that the accuracy of the present LBE-KBC method is compatible to the 2D finite-volume scheme. In Figures 15 and 16, the numerical results are compared

Table V. Comparison of simulation and theory with different models

Scenario	Period difference (%)		Wave height difference (%)		Nonlinear wave shape difference (%)	
	LBE-KBC	FVM	LBE-KBC	FVM	LBE-KBC	FVM
1	0.078	0.32	0.97	1.10	2.10	0.31
2	0.230	0.23	0.12	0.64	0.70	0.22
3	11	11	3.80	0.64	0.33	0.12
4	0.450	0.87	0.90	1.10	0.76	0.37
5	0.520	0.87	0.46	3.70	1.20	0.32

‘Period difference’, means the difference between the simulated and theoretical wave period for the four oscillations simulated, and is expressed as a percentage of the theoretical period;

‘wave height difference’, the RMS difference between the simulated and theoretical wave height for the four periods and is expressed as a percentage of the theoretical wave height;

‘wave shape difference’, the RMS difference between the simulated wave shape and theory for one wave, expressed as a percentage of the wave height, and measured at the second wave period for scenario 3 and the fourth wave period for all other scenarios.

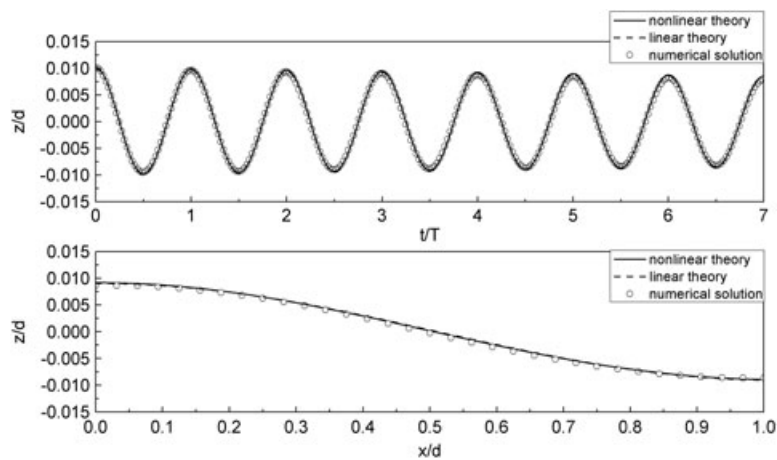


Figure 15. Comparison of free surface elevation of the numerical solution with nonlinear and linear analytical solution in scenario 2: the time series of free surface elevation on the left side wall (top); and the wave shape at $t=4T$ (bottom).

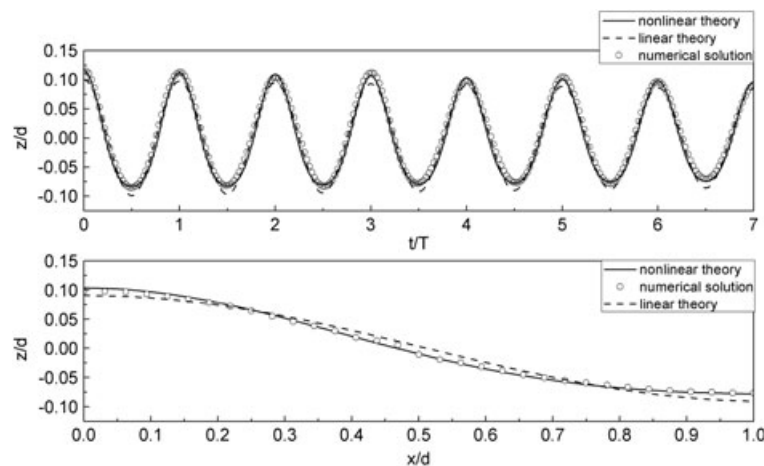


Figure 16. Comparison of free surface elevation of the numerical solution with nonlinear and linear analytical solution in scenario 5: the time series of free surface elevation on the left side wall (top); and the wave shape at $t=4T$ (bottom).

with both the nonlinear analytical solution and linear analytical solution for scenario 2 and scenario 5, respectively. It can be seen that the numerical wave shapes are closer to the theoretical nonlinear shapes than to the linear shapes, especially for the finite amplitude waves in scenario 5.

3.4. Small amplitude Stokes waves

The LBE–KBC method is further tested by simulation of small amplitude Stokes waves propagating along a 960-m long, $d = 15$ -m deep wave flume, which is frequently used to validate their models accuracy [53,54]. A wave maker that generates the sinusoidal velocity distribution is used at the left boundary [54],

$$u = \begin{cases} 0, & t = 0, \\ a\omega \sin(\omega t), & t > 0, \end{cases} \quad (45)$$

where a is the wave amplitude and ω is the circular frequency. Then, the free surface water elevation of the small amplitude Stokes waves can be written as,

$$\eta(x, t) = a \cos(kx - \omega t) + \frac{\pi a^2}{2l} \left(1 + \frac{3}{2 \sinh^2 kd} \right) \coth(kd) \cos(2kx - 2\omega t) + d, \quad (46)$$

where k is the wave number, ω is the wave frequency and l is the wave length. The wave amplitude, wave period and wave length here are 0.3 m, 4.5 s and 31.62 m, respectively. In the computation, $\delta x = \delta y = 0.5$ m and $e = 40$ m/s, the LB viscosity $\tau = 0.500000171$ (the kinematic viscosity $\nu = 1.14 \times 10^{-6}$ m²/s), $\text{Ma} = \frac{\sqrt{3}a\omega}{e} = 0.018$, $\text{Re} = la\omega/\nu = 1.16 \times 10^5$ and $\text{Fr} = a\omega/\sqrt{gl} = 0.024$. To investigate grid convergence, three different meshes of 768×20 , 960×20 , and 1280×20 are used. In the horizontal direction, three different grid sizes are used: $dX = 2.5\delta x$, $2\delta x$, $1.5\delta x$. In the vertical direction, a grid size $dY = \delta y$ is adopted near the water surface, and a grid size $dY = 4\delta y$ is used in the rest of the domain.

Figure 17 shows the comparison of predicted and analytical free surface elevation along 0–300 m, at $t = 138.5$ s. It can be seen that the numerical results with different meshes compare favorably with the analytical solution, with the good agreements of wave celerity, wavelength and wave amplitude. Among different meshes, the mesh of 1280×20 leads to the most accurate result. In Figure 18, predicted free surface elevations by the mesh of 1280×20 at three different stations ($x = 10, 100$ and 200 m from the position of the wave paddle) are compared with the corresponding analytical results. We can find the satisfactory agreement, which indicates that the wave period is also correctly predicted.

3.5. Wave traveling over a submerged bar

In order to examine the performance of the proposed method in modeling wave deformation over uneven bottoms, the wave traveling over a submerged bar is selected as the last example. In this case, the incoming waves on the upward slope is shoaling, with nonlinearity generating bounded higher harmonic waves, which travel phase-locked to the primary wave; on the downward slope, these harmonic waves are released as free waves. Many researchers have paid a great deal of effort to investigate this process using physical experiments or numerical simulations [34, 53, 55].

In the computational domain, sketched in Figure 19, the velocity at the inlet boundary is prescribed in terms of linear wave theory; at the outflow boundary, one wave length sponge layer with a rigid boundary is applied. The incident wave height is 0.02 m, and the wave period is 2 s. The set-up is the same as that used in the experiment reported by Beji and Battjes [55]. $\delta x = \delta y = 0.0125$ m and $e = 3$ m/s, the LB viscosity $\tau = 0.5000912$ (the kinematic viscosity $\nu = 1.14 \times 10^{-6}$ m²/s), $\text{Ma} = \frac{\sqrt{3}a\omega}{e} = 0.018$, $\text{Re} = \frac{la\omega}{\nu} = 1.72 \times 10^5$ and $\text{Fr} = a\omega/\sqrt{gl} = 0.0040$. There are 28 cells and 1100 cells in the vertical and horizontal directions, respectively. Vertically, fine grids ($dY = \delta x$) and coarse grids ($dY = 2\delta x$) are adopted near the water surface and at the other domain, respectively. In the horizontal direction, the grid size $dX = 2\delta x$.

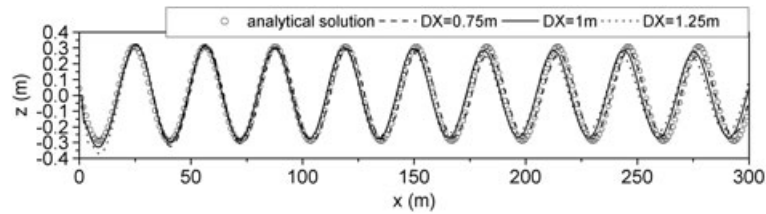


Figure 17. Convergence of free surface elevation along 0–300 m, at $t = 138.5$ s.

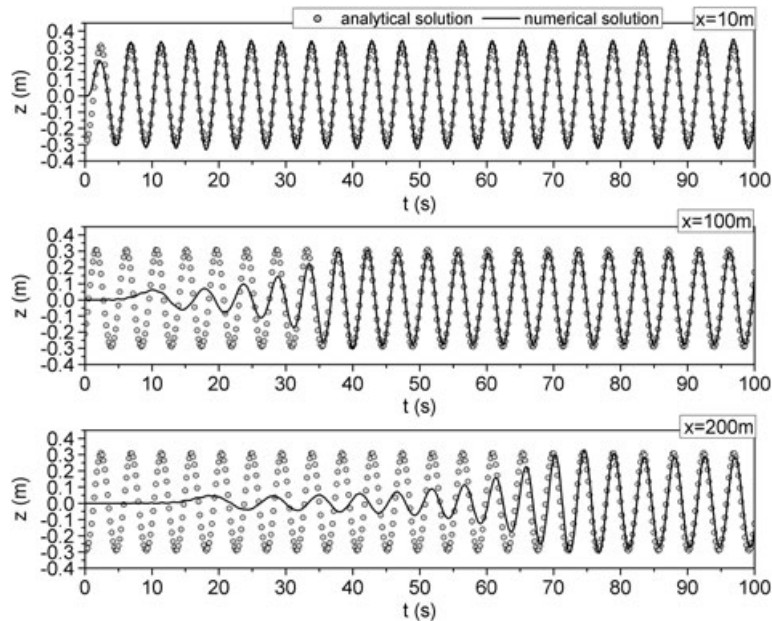


Figure 18. Comparison of free surface elevation of the numerical solution with analytical solution at three different stations ($x = 10, 100$ and 200 m).

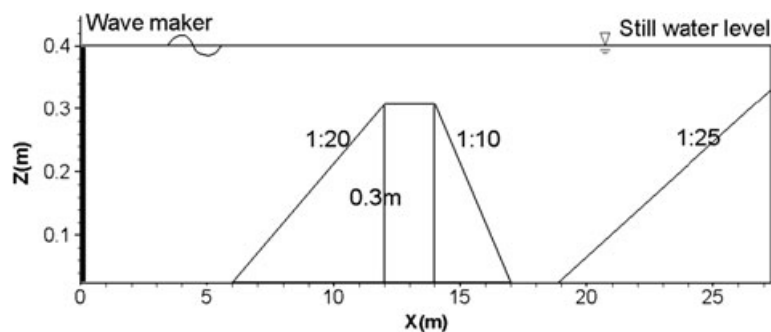


Figure 19. Experimental layout for wave traveling over a submerged bar.

Figure 20 shows a comparison of free surface elevation with experimental data at six different stations. It indicates that the LBE–KBC method satisfactorily simulates the shoaling phenomenon at the first two stations. As the wave rides over the bar, the development of higher frequency components at locations $x = 13.5$ m and $x = 14.5$ m is also well simulated. The release of generated higher frequency components occurring behind the bar at locations $x = 15.7$ m and $x = 17.3$ m is

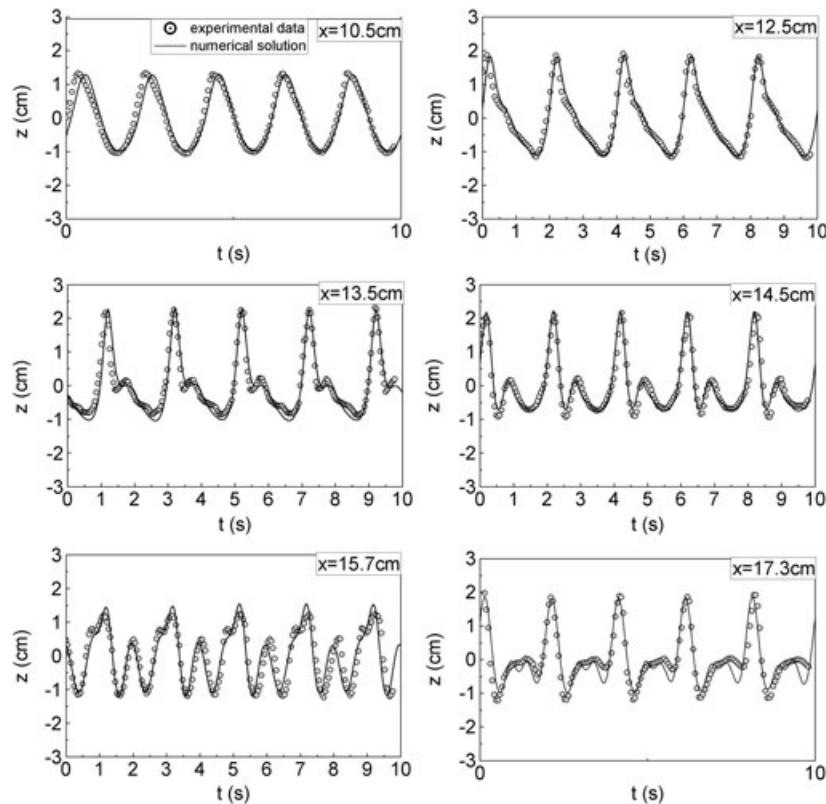


Figure 20. Time series of the simulated free surface elevations at six different stations and the comparison with experimental data.

also well predicted. The overall good agreements in free surface elevation indicate that the present LBE–KBC method can accurately simulate wave shoaling, nonlinearity, and dispersion phenomena.

The numerical results for free surface profiles along the wave tank at an interval of 1 s are shown in Figure 21. It can be seen that as the harmonic waves propagate over the bar, the primary wave crests become steeper, and a dispersive tail gradually develops. A small wave appears at the trailing edge of a primary wave. This small wave propagates slower than the main wave and gradually detaches from the main crest. Then, the small wave is overtaken by the next wave. These phenomena are quite consistent with previous observations [34, 53, 55].

3.6. Performance

The LBE–KBC scheme has several parts, which may contribute to the runtime: (1) collision and forcing; (2) FSBC; (3) other BC; (4) streaming and ISLB; (5) \mathbf{u} , p_D calculation; (6) η^{n+1} calculation; and (7) states change. Table VI shows the average runtime percentage of every part for the four test cases, from which we can see that only about 6% of the total runtime is used by the steps of η calculation and states change, and about 65% ~ 80% is consumed by the steps of collision, forcing, streaming and ISLB. It indicates that less runtime is needed by the additional steps for the free surface problem (η calculation and states change). In order to measure the performance of LBE–KBC scheme, the mega lattice updates per second (MLUPS) has been used, and all test cases have been performed on a ThinkPad R400 Levono (Singapore) machine with an Intel Core Duo 2.66 GHz CPU (Intel, STa. Clara, CA, USA). The MLUPS are determined from the ratio of the total number of cells in which the collision step is performed when simulating one time step and the corresponding runtime of the simulation. The runtimes per time step (in seconds) are also measured. In Table VII, the performance in MLUPS and the runtimes per time step for different test cases mentioned in the previous sections is given. For comparison, the performance of a standard BGK LB code, which simulates the lid driven flow presented in [56] is also given. The MLUPS rate of

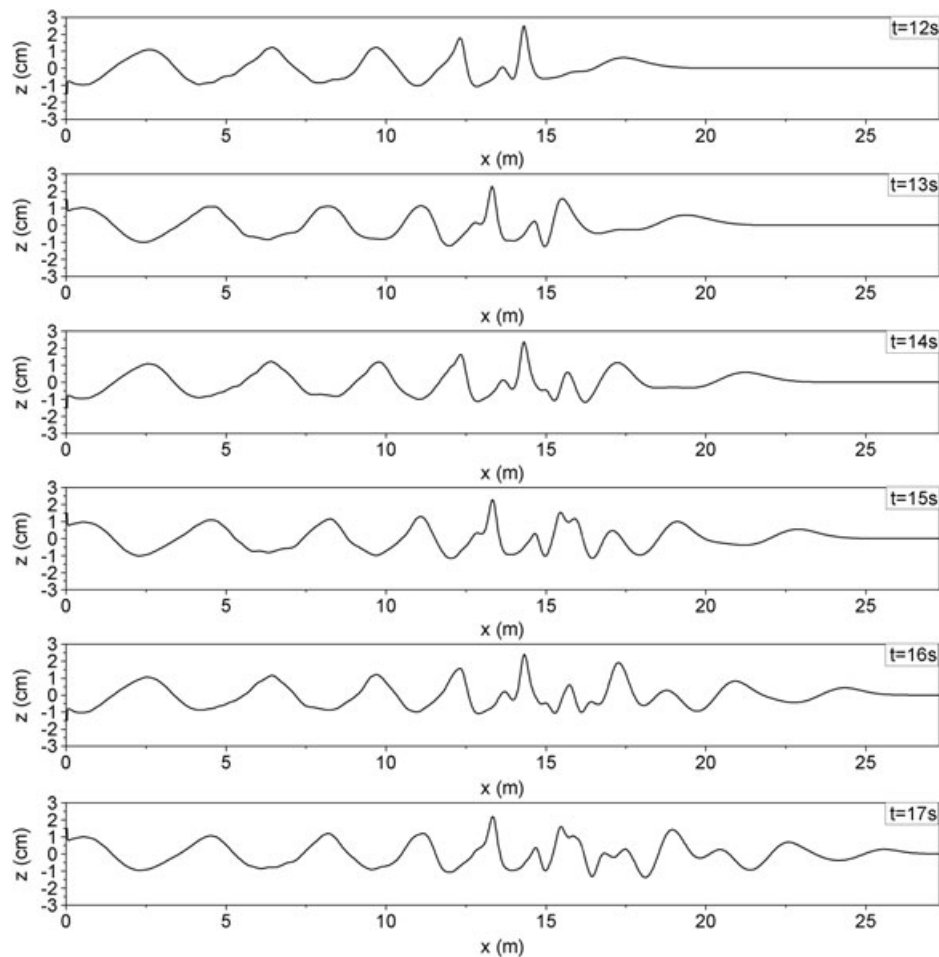


Figure 21. The wave shapes along the wave tank at several time instants.

Table VI. Runtime percentage of every part of LBE–KBC scheme for the four test cases.

Runtime percentage (%)	Collision and forcing	FSBC	Other BC	Streaming and ISLB	u, p_D calculation	η^{n+1} calculation	States change
Case 2	44.95	10.54	6.71	24.61	7.06	1.00	5.39
Case 3	42.26	4.78	11.04	27.67	7.34	0.93	5.97
Case 4	45.43	2.23	3.98	35.20	7.09	0.82	5.25
Case 5	33.26	1.84	22.65	32.44	5.31	0.68	3.82

LBE–KBC, lattice Boltzmann equation–kinematic boundary condition; FSBC, free surface boundary condition; ISLB, interpolation-supplemented lattice Boltzmann.

LBE–KBC scheme with best results on Case 3 is about three times lower compared with the standard BGK LB code. Because of the adoption of the MRT model and the ISLB method in LBE–KBC scheme, it really increases the runtime. However, the LBE–KBC scheme is more stable and flexible. Moreover, as the mesh grids are nonuniform, the total number of mesh grids can be reduced, which finally save the simulation time. Compared with other nonuniform mesh grid LB scheme, it is worth noticing that the MLUPS rate of the best results of our scheme is 1.6 times higher than that of the BGK LB on octree-like grids presented in [57] (performed on a 64-bit i7 quad core machine with 2.80 GHz and an 8-MB / 256-kB L3/L2 cache).

Table VII. The MLUPS and measured runtimes per time step.

Case	Total no. of cells	MLUPS	Runtime/time step (s)
Case 2	400×12	1.040	0.00383
Case 3	32×25	1.209	0.00060
Case 4	1280×20	1.030	0.02110
Case 5	1100×28	0.936	0.03132
Lid driven flow (standard BGK)	256×256	3.655	0.01793
Lid driven flow (presented in [57])	6561	0.750	0.00875

MLUPS, mega lattice updates per second; BGK, Bhatnagar–Gross–Krook.

4. CONCLUSION

In this work, the LBE–KBC method for simulating 2D viscous free surface wave problem is proposed, based on the combination of the lattice Boltzmann equations for flows and kinematic boundary condition method for free surface. In our method, only the non-hydrostatic pressure is included in the equilibrium distribution functions. The hydrostatic part, which is expressed as a function of free surface elevation, is added as a force term to the LBE with a finite difference scheme. The former-FSBC is revised to enhance the accuracy of the results in the coarse grid systems. With the ISLB method, the scheme is successfully applied on arbitrary, nonuniform mesh grids, and therefore, the computational efficiency of the LBE–KBC method is much enhanced.

The proposed LBE–KBC method is verified by five cases: the stationary flow, the standing waves, the solitary wave, small amplitude Stokes waves and traveling waves over a submerged bar. The results indicate the following: (1) modeling results obtained by the revised-FSBC are more accurate than the one obtained by the former-FSBC especially in coarse grid systems; (2) the LBE–KBC method is compatible to the 2D finite-volume scheme; and (3) simulated results of the proposed method are in good agreement with existing theory and experimental observations in wave celerity, wavelength, wave amplitude and wave period. They indicate that the LBE–KBC method has the ability to model complex wave deformation problems. This method is proven to be convenient for moderate non-breaking waves, and it is easy to implement, computationally efficient, and it requires minimum memory storage. The present LBE–KBC method can be used to solve more complex practical problem and easily extended to three dimensions. Such extension and applications will be considered in future studies.

APPENDIX A: OBTAINMENT OF THE REVISED-FSBC

For a free surface problem (Figure A.1), the momentum fluxes between E-cell and I-cell or I-cell and I-cell are considered. For simplicity, a condition of $-0.5 \leq \frac{\partial \eta}{\partial x} < 0.5$ is selected as a specific case; however, similar deducing processes can be found in other cases.

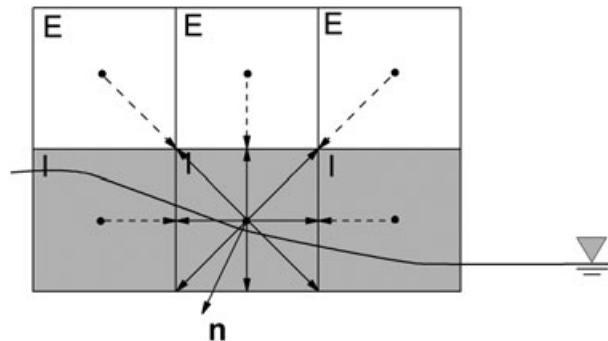


Figure A.1. Momentum flux between E-cell and I-cell or I-cell and I-cell.

In the normal direction, the momentum fluxes can be calculated as follows:

$$\begin{aligned}
 I_{\alpha}^n &= n_{\beta} A(\mathbf{x}) \\
 &\times \left[\sum_{i, \mathbf{n} \cdot \mathbf{e}_i < 0 \text{ or State}(\mathbf{x} - \mathbf{e}_i) = \text{I-cell}} f_i'(\mathbf{x}, t) \mathbf{e}_{i,\alpha} \mathbf{e}_{i,\beta} + \sum_{I, \mathbf{n} \cdot \mathbf{e}_i < 0 \text{ or State}(\mathbf{x} - \mathbf{e}_i) = \text{I-cell}} f_I'(\mathbf{x} - \mathbf{e}_I, t) \mathbf{e}_{I,\alpha} \mathbf{e}_{I,\beta} \right] \\
 &= n_{\beta} A(\mathbf{x}) \sum_{i, \mathbf{n} \cdot \mathbf{e}_i < 0 \text{ or State}(\mathbf{x} - \mathbf{e}_i) = \text{I-cell}} f_i'(\mathbf{x}, t) \mathbf{e}_{i,\alpha} \mathbf{e}_{i,\beta} \\
 &\quad + n_{\beta} A(\mathbf{x}) \sum_{I, \mathbf{n} \cdot \mathbf{e}_i < 0 \text{ and State}(\mathbf{x} - \mathbf{e}_i) \neq \text{I-cell}} [f_I^{eq} + f_i^{eq} - f_i'(\mathbf{x}, t)] \mathbf{e}_{I,\alpha} \mathbf{e}_{I,\beta} \\
 &\quad + n_{\beta} A(\mathbf{x}) \sum_{I, \text{State}(\mathbf{x} - \mathbf{e}_i) = \text{I-cell}} f_I'(\mathbf{x} - \mathbf{e}_I, t) \mathbf{e}_{I,\alpha} \mathbf{e}_{I,\beta} \\
 &= n_{\beta} A(\mathbf{x}) \sum_{i, \text{State}(\mathbf{x} - \mathbf{e}_i) = \text{I-cell}} \left[f_i'(\mathbf{x}, t) \mathbf{e}_{i,\alpha} \mathbf{e}_{i,\beta} + f_I'(\mathbf{x} - \mathbf{e}_I, t) \mathbf{e}_{I,\alpha} \mathbf{e}_{I,\beta} \right] \\
 &\quad + n_{\beta} A(\mathbf{x}) \left[\delta_{\alpha,\beta} p_D + u_{\alpha} u_{\beta} - \sum_{I, \mathbf{n} \cdot \mathbf{e}_i < 0 \text{ and State}(\mathbf{x} - \mathbf{e}_i) = \text{I-cell}} (f_I^{eq} + f_i^{eq}) \mathbf{e}_{I,\alpha} \mathbf{e}_{I,\beta} \right]. \quad (\text{A.1})
 \end{aligned}$$

The first term of the result of Equation (A.1) can be seen as the momentum fluxes of the fluid between the I-cells; the second term is the momentum fluxes between the I-cell and G-cell. In the former-FSBC, it has

$$\sum_{I, \mathbf{n} \cdot \mathbf{e}_i < 0 \text{ and State}(\mathbf{x} - \mathbf{e}_i) = \text{I-cell}} \left\{ -[f_I^{eq} + f_i^{eq}] + f_i'(\mathbf{x}, t) + f_I'(\mathbf{x} - \mathbf{e}_I, t) \right\} = 0, \quad (\text{A.2})$$

then

$$\begin{aligned}
 I_{\alpha}^n &= n_{\beta} A(\mathbf{x}) \left\{ \sum_{i, \mathbf{n} \cdot \mathbf{e}_i \leq 0 \text{ and State}(\mathbf{x} - \mathbf{e}_i) = \text{I-cell}} [f_i'(\mathbf{x}, t) \mathbf{e}_{i,\alpha} \mathbf{e}_{i,\beta} + f_I'(\mathbf{x} - \mathbf{e}_I, t) \mathbf{e}_{I,\alpha} \mathbf{e}_{I,\beta}] \right\} \\
 &\quad + n_{\beta} A(\mathbf{x}) \delta_{\alpha,\beta} p_D + n_{\beta} A(\mathbf{x}) u_{\alpha} u_{\beta}. \quad (\text{A.3})
 \end{aligned}$$

It can be seen that for the former-FSBC, the normal pressure is fulfilled, whereas the momentum fluxes of fluid between the I-cells in the direction \mathbf{I} with $\mathbf{n} \cdot \mathbf{e}_i < 0$ are not satisfied as the additional condition of Equation (A.2) must be met. In fact, they are treated as E-cells during the reconstruction. However, it is worth noticing that the momentum flux between the I-cells in the direction \mathbf{I} with $\mathbf{n} \cdot \mathbf{e}_i < 0$ is also important because it contains the momentum flux of fluid. The main difference between the revised-FSBC and the former-FSBC is that the revised-FSBC fully considers the momentum fluxes of fluid. For the revised-FSBC, the information coming from the neighboring I-cells are fully taken into account without the condition of Equation (A.2). In fact, if $\mathbf{n} = (0, -1)$, we have $n_{\beta} \mathbf{e}_{1,\alpha} \mathbf{e}_{1,\beta} = \mathbf{0}$, $n_{\beta} \mathbf{e}_{2,\alpha} \mathbf{e}_{2,\beta} = \mathbf{0}$. The reconstruction in the directions 1 and 2 is of no effect to the normal non-hydrostatic pressure. Equation (A.1) becomes

$$I_{\alpha}^n = n_{\beta} A(\mathbf{x}) (\delta_{\alpha,\beta} p_D + u_{\alpha} u_{\beta}). \quad (\text{A.4})$$

It means that both the normal pressure at the free surface and the momentum fluxes of fluid between the I-cells are exactly satisfied without considering Equation (A.2) (revised-FSBC), under which the revised-FSBC leads to a most accurate result in theory. Accordingly, the distribution functions coming from the neighboring I-cell with $n_{\beta} \mathbf{e}_{i,\alpha} \mathbf{e}_{i,\beta} \approx \mathbf{0}$ are not reconstructed, not affecting the free surface non-hydrostatic pressure too much but fully taking account of the momentum flux between the I-cells. It is the key point of the revised-FSBC. Now, the problem is to find the directions with the minimum value of $n_{\beta} \mathbf{e}_{i,\alpha} \mathbf{e}_{i,\beta}$ among the eight directions.

To evaluate the ratio of $n_\beta \mathbf{e}_{i,\alpha} \mathbf{e}_{i,\beta}$ and $\tau_\beta \mathbf{e}_{i,\alpha} \mathbf{e}_{i,\beta}$ in different lattice direction i , here, we write $n_\beta \mathbf{e}_{i,\alpha} \mathbf{e}_{i,\beta}$ and $\tau_\beta \mathbf{e}_{i,\alpha} \mathbf{e}_{i,\beta}$ in the interface coordinate system $\{x, y\} = \{n, \tau\}$, such that the normal vector and tangential vector are $\mathbf{n} = (n_n, 0)$, $\tau = (0, \tau_\tau)$, we have

$$n_n \mathbf{e}_{i,n} \mathbf{e}_{i,n} = \begin{cases} \frac{(\partial\eta/\partial x)^2}{1+(\partial\eta/\partial x)^2}, & i = 1, 2 \\ \frac{1}{1+(\partial\eta/\partial x)^2}, & i = 3, 4 \\ \frac{(1-\partial\eta/\partial x)^2}{1+(\partial\eta/\partial x)^2}, & i = 5, 6 \\ \frac{(1+\partial\eta/\partial x)^2}{1+(\partial\eta/\partial x)^2}, & i = 7, 8 \end{cases} \quad (\text{A.5})$$

$$\tau_\tau \mathbf{e}_{i,\tau} \mathbf{e}_{i,\tau} = \begin{cases} \frac{1}{1+(\partial\eta/\partial x)^2}, & i = 1, 2 \\ \frac{\partial\eta/\partial x}{1+(\partial\eta/\partial x)^2}, & i = 3, 4 \\ \frac{(1+\partial\eta/\partial x)^2}{1+(\partial\eta/\partial x)^2}, & i = 5, 6 \\ \frac{(1-\partial\eta/\partial x)^2}{1+(\partial\eta/\partial x)^2}, & i = 7, 8 \end{cases} \quad (\text{A.6})$$

We defined $N = \sum_{i=1,3,5,7} n_n \mathbf{e}_{i,n} \mathbf{e}_{i,n}$ and $M = \sum_{i=1,3,5,7} \tau_\tau \mathbf{e}_{i,\tau} \mathbf{e}_{i,\tau}$. In fact, if $\frac{\partial\eta}{\partial x} = 0.5$, direction $i=1$ (or 2) and direction $i=5$ (or 6) have the same value of $n_\beta \mathbf{e}_{i,\alpha} \mathbf{e}_{i,\beta}$. It is taken as the demarcation point between direction $i=1$ (or 2) and direction $i=5$ (or 6). Similarly, the other demarcation points can be found for different directions. Five types of conditions are classified according to the demarcation points:

1. $-0.5 \leq \frac{\partial\eta}{\partial x} < 0.5$, the directions $i=1, 2$ have the distribution functions coming from the I-cells. Table A.1 shows that the lattice directions $i=1$ (or 2) has the maximum ratio of 6.67% in normal direction and the minimum ratio of 26.67% in tangential direction. It shows that the direction $i=1, 2$ have a more important effect on the tangential direction than that on the normal direction.
2. $0.5 \leq \frac{\partial\eta}{\partial x} < 2$, the directions $i=5, 6$ have the distribution functions coming from the I-cell. Table A.2 shows that the lattice directions $i=5$ (or 6) has the maximum ratio of 6.67% in normal direction and the minimum ratio of 60.00% in tangential direction. It shows that the direction $i=5, 6$ have a more important effect on the tangential direction than that on the normal direction.
3. $2 \leq \frac{\partial\eta}{\partial x}$, the directions $i=3, 4$ have the distribution functions coming from the I-cell. Table A.3 shows that the lattice directions $i=3$ (or 4) has the maximum ratio of 6.67% in normal direction and the minimum ratio of 26.67% in tangential direction. It shows that the direction $i=3, 4$ have a more important effect on the tangential direction than that on the normal direction.
4. $-2 \leq \frac{\partial\eta}{\partial x} < -0.5$, the directions $i=7, 8$ have the distribution functions coming from the I-cell. Table A.4 shows that the lattice directions $i=7$ (or 8) has the maximum ratio of 6.67% in normal direction and the minimum ratio of 60.00% in tangential direction. It shows that the direction $i=7, 8$ have a more important effect on the tangential direction than that on the normal direction.
5. $\frac{\partial\eta}{\partial x} < -2$, the directions $i=3, 4$ have the distribution functions coming from the I-cell. Table A.5 shows that the lattice directions $i=3$ (or 4) has the maximum ratio of 6.67% in normal direction and the minimum ratio of 26.67% in tangential direction. It shows that the direction $i=3, 4$ have a more important effect on the tangential direction than that on the normal direction.

It can be seen that for the revised-FSBC, the maximum ratio of $n_n \mathbf{e}_{i,n} \mathbf{e}_{i,n}$ with $\text{State}(\mathbf{x} - \mathbf{e}_i) = \text{I-cell}$ and $\mathbf{n} \cdot \mathbf{e}_i > 0$ is 6.67%, which is smaller than the other lattice directions. So in the revised-FSBC, the distribution functions which have the minimum ratio of $n_n \mathbf{e}_{i,n} \mathbf{e}_{i,n}$ (compared with other lattice directions) with $\text{State}(\mathbf{x} - \mathbf{e}_i) = \text{I-cell}$ and $\mathbf{n} \cdot \mathbf{e}_i > 0$ are not reconstructed. It minimizes the errors of the non-hydrostatic pressure at the free surface and fully satisfies the momentum fluxes between the I-cells.

Table A.1. The value of $\max(n_n \mathbf{e}_{i,n} \mathbf{e}_{i,n} / N)$ and $\min(\tau_\tau \mathbf{e}_{i,\tau} \mathbf{e}_{i,\tau} / M)$ when $-0.5 \leq \frac{\partial \eta}{\partial x} < 0.5$.

Lattice direction	$\max(n_n \mathbf{e}_{i,n} \mathbf{e}_{i,n} / N) (\%)$	$\min(\tau_\tau \mathbf{e}_{i,\tau} \mathbf{e}_{i,\tau} / M) (\%)$
$i = 1$ (or 2)	6.67	26.67
$i = 3$ (or 4)	33.33	0.00
$i = 5$ (or 6)	60.00	6.67
$i = 7$ (or 8)	60.00	6.67

Table A.2. The value of $\max(n_n \mathbf{e}_{i,n} \mathbf{e}_{i,n} / N)$ and $\min(\tau_\tau \mathbf{e}_{i,\tau} \mathbf{e}_{i,\tau} / M)$ when $0.5 \leq \frac{\partial \eta}{\partial x} < 2$.

Lattice direction	$\max(n_n \mathbf{e}_{i,n} \mathbf{e}_{i,n} / N) (\%)$	$\min(\tau_\tau \mathbf{e}_{i,\tau} \mathbf{e}_{i,\tau} / M) (\%)$
$i = 1$ (or 2)	26.67	6.67
$i = 3$ (or 4)	26.67	6.67
$i = 5$ (or 6)	6.67	60.00
$i = 7$ (or 8)	60.00	6.67

Table A.3. The value of $\max(n_n \mathbf{e}_{i,n} \mathbf{e}_{i,n} / N)$ and $\min(\tau_\tau \mathbf{e}_{i,\tau} \mathbf{e}_{i,\tau} / M)$ when $2 \leq \frac{\partial \eta}{\partial x}$.

Lattice direction	$\max(n_n \mathbf{e}_{i,n} \mathbf{e}_{i,n} / N) (\%)$	$\min(\tau_\tau \mathbf{e}_{i,\tau} \mathbf{e}_{i,\tau} / M) (\%)$
$i = 1$ (or 2)	33.33	0.00
$i = 3$ (or 4)	6.67	26.67
$i = 5$ (or 6)	33.33	33.33
$i = 7$ (or 8)	60.00	6.67

Table A.4. The value of $\max(n_n \mathbf{e}_{i,n} \mathbf{e}_{i,n} / N)$ and $\min(\tau_\tau \mathbf{e}_{i,\tau} \mathbf{e}_{i,\tau} / M)$ when $-2 \leq \frac{\partial \eta}{\partial x} < -0.5$.

Lattice direction	$\max(n_n \mathbf{e}_{i,n} \mathbf{e}_{i,n} / N) (\%)$	$\min(\tau_\tau \mathbf{e}_{i,\tau} \mathbf{e}_{i,\tau} / M) (\%)$
$i = 1$ (or 2)	26.67	6.67
$i = 3$ (or 4)	26.67	6.67
$i = 5$ (or 6)	60.00	6.67
$i = 7$ (or 8)	6.67	60.00

Table A.5. The value of $\max(n_n \mathbf{e}_{i,n} \mathbf{e}_{i,n} / N)$ and $\min(\tau_\tau \mathbf{e}_{i,\tau} \mathbf{e}_{i,\tau} / M)$ when $\frac{\partial \eta}{\partial x} < -2$.

Lattice direction	$\max(n_n \mathbf{e}_{i,n} \mathbf{e}_{i,n} / N) (\%)$	$\min(\tau_\tau \mathbf{e}_{i,\tau} \mathbf{e}_{i,\tau} / M) (\%)$
$i = 1$ (or 2)	33.33	0.00
$i = 3$ (or 4)	6.67	26.67
$i = 5$ (or 6)	60.00	6.67
$i = 7$ (or 8)	33.33	33.33

ACKNOWLEDGEMENTS

The authors gratefully thank Dr. Shaotian Li for his language support and valuable discussions, and Dr. Zhiyong Wu for his useful suggestion.

REFERENCES

1. Peregrine DH. Long waves on a beach. *Journal of Fluid Mechanics* 1967; **27**:815–827.
2. Berkhoff JCW. Computation of combined refraction–diffraction. *Coastal Engineering*, Vancouver, Canada, 1972; 471–491.
3. Madsen PA, Sørensen OR. A new form of the Boussinesq equations with improved linear dispersion characteristics. *II: A slowly-varying bathymetry* 1992; **18**:371–388.

4. Nwogu O. Alternative form of Boussinesq equations for nearshore wave propagation. *Journal of Waterway, Port, Coastal, and Ocean Engineering* 1993; **119**:618–638.
5. Chen Y, Liu FPL. Modified Boussinesq equations and associated parabolic models for water wave propagation. *Journal of Fluid Mechanics* 1995; **288**:351–381.
6. Wei GE, Kirby TJ, Grilli TS, Subramanya R. A fully nonlinear Boussinesq model for surface waves. I: Highly nonlinear unsteady waves. *Journal of Fluid Mechanics* 1995; **294**:71–92.
7. Gobbi FM, Kirby TJ, Wei GE. A fully nonlinear Boussinesq model for surface waves. Part 2. Extension to $O(kh)$. *Journal of Fluid Mechanics* 2000; **405**:181–210.
8. Hsiao SC, Lynett P, Hwung HH, Liu PLF. Numerical simulations of nonlinear short waves using a multilayer model. *Journal of Engineering Mechanics* 2005; **131**:231–243.
9. Kirby JT, Dalrymple RA. A parabolic equation for the combined refraction–diffraction of Stokes waves by mildly varying topography. *Journal of Fluid Mechanics* 1983; **136**:453–466.
10. Kaihatu JM, Kirby JT. Nonlinear transformation of waves in finite water depth. *Physics of Fluids* 1995; **7**:1903–1914.
11. Tang Y, Ouellet Y. A new kind of nonlinear mild-slope equation for combined refraction–diffraction of multifrequency waves. *Coastal Engineering* 1997; **31**:3–36.
12. Turnbull MS, Borthwick AGL, Eatock Taylor R. Numerical wave tank based on a sigma-transformed finite element inviscid flow solver. *International Journal for Numerical Methods in Fluids* 2003; **42**:641–663.
13. Bai W, Eatock Taylor R. Higher-order boundary element simulation of fully nonlinear wave radiation by oscillating vertical cylinders. *Applied Ocean Research* 2006; **28**:247–265.
14. Bai W, Eatock Taylor R. Numerical simulation of fully nonlinear regular and focused wave diffraction around a vertical cylinder using domain decomposition. *Applied Ocean Research* 2007; **29**:55–71.
15. Hodges BR, Street RL, Zang Y. A method for simulation of viscous, non-linear, free-surface flows. In *20th Sym. on Naval Hydrodynamics*. Nat'l. Acad. Press: Washington, D.C., 1996; 791–809.
16. Tang CT, Patel VC, Landweber L. Viscous effects on propagation and reflection of solitary waves in shallow channels. *Journal of Computational Physics* 1990; **88**:86–113.
17. Wang HW, Huang CJ, Wu J. Simulation of a 3D numerical viscous wave tank. *Journal of Engineering Mechanics* 2007; **133**:761–772.
18. Sterling JD, Chen SY. Stability analysis of lattice Boltzmann methods. *Journal of Computational Physics* 1996; **123**:196–206.
19. Filippova O, Succi S, Mazzocco F, Arrighetti C, Bella G, Hänel D. Multiscale lattice Boltzmann schemes with turbulence modeling. *Journal of Computational Physics* 2001; **170**:812–829.
20. Yu H, Girimaji SS, Luo L. DNS and LES of decaying isotropic turbulence with and without frame rotation using lattice Boltzmann method. *Journal of Computational Physics* 2005; **209**:599–616.
21. Eggels JGM, Somers JA. Numerical simulation of free convective flow using the lattice Boltzmann scheme. *International Journal of Heat and Fluid Flow* 1995; **16**:357–364.
22. Li YN, Huang P. A coupled lattice Boltzmann model for advection and anisotropic dispersion problem in shallow water. *Advances in Water Resources* 2008; **31**:1719–1730.
23. Li YN, Huang P. A coupled lattice Boltzmann model for the shallow water-contamination system. *International Journal for Numerical Methods in Fluids* 2009; **59**:195–213.
24. Rothman DH, Keller JM. Immiscible cellular-automaton fluids. *Journal of Statistical Physics* 1988; **52**:1119.
25. Shan X, Doolen G. Multicomponent lattice-Boltzmann model with interparticle interaction. *Journal of Statistical Physics* 1995; **81**:379.
26. Thürey N, Rüde U. Free surface lattice-Boltzmann fluid simulations with and without Level Sets, 2004; 199–208.
27. Thürey N, Rüde U, Körner C. Interactive free surface fluids with the lattice Boltzmann method. *University of Erlangen-Nuremberg, Department of Computer Science 10, System Simulation(LSS) Technical Report 05-4*, Department of Computer Science 10 System Simulation, University of Erlangen-Nuremberg, 2005.
28. Körner C, Thies M, Hofmann T, Thürey N, Rüde U. Lattice Boltzmann model for free surface flow for modeling foaming. *Journal of Statistical Physics* 2005; **121**:179–196.
29. Janssen C, Krafczyk M. A lattice Boltzmann approach for free-surface-flow simulations on non-uniform block-structured grids. *Computers & Mathematics with Applications* 2010; **59**:2215–2235.
30. Gunstensen AK, Rothman DH. Microscopic modeling of immiscible fluids in three dimensions by a lattice Boltzmann method. *Europhysics Letters* 1992; **18**:157–161.
31. He XY, Chen SY, Zhang RY. A lattice Boltzmann scheme for incompressible multiphase flow and its application in simulation of Rayleigh–Taylor instability. *Journal of Computational Physics* 1999; **152**:642–663.
32. Casulli V. A semi-implicit finite difference method for non-hydrostatic, free-surface flows. *International Journal for Numerical Methods in Fluids* 1999; **30**:425–440.
33. Demirel E, Aydin I. Global volume conservation in unsteady free surface flows with energy absorbing far-end boundaries. *International Journal for Numerical Methods in Fluids* 2010; **64**:689–708.
34. Bai W, Mingham CG, Causon DM, Qian L. Finite volume simulation of viscous free surface waves using the Cartesian cut cell approach. *International Journal for Numerical Methods in Fluids* 2009; **63**:69–95.
35. Ai CF, Jin S, Lv B. A new fully non-hydrostatic 3D free surface flow model for water wave motions. *International Journal for Numerical Methods in Fluids* 2010; **66**:1354–1370.
36. Chan RKC, Street RL. SUMMACA numerical model for water waves. *Technical Report 135*, 1970.

37. Hino T, Martinelli L, Jameson A. A finite-volume method with unstructured grid for free surface flow simulations. In *The Sixth International Conference on Numerical Ship Hydrodynamics*. Ship Research Institute: Tokyo, Japan, 1993.
38. Loh YC, Rasmussen H. A numerical procedure for viscous free surface flows. *Applied Numerical Mathematics* 1987; **3**:479–495.
39. Dommermuth GD. The laminar interactions of a pair of vortex tubes with a free surface. *Journal of Fluid Mechanics* 1993; **246**:91–115.
40. Hinatsu M. Numerical simulation of unsteady viscous nonlinear waves using moving grid system fitted on a free surface. *Journal of the Kansai Society of Naval Architects* 1992; **217**:1–11.
41. Ohring S, Lugt HJ. Two counter-rotating vortices approaching a free surface in a viscous fluid. *Final Report Naval Ship Research and Development Center, Bethesda, MD*, 1989.
42. Kassinos AC, Prusa J. A numerical model for 3D viscous sloshing in moving containers. *Recent Advances and Applications in Computational Fluid Dynamics* 1990; **FED-103**:75–86.
43. He XY, Luo LS, Dembo M. Some progress in lattice Boltzmann method. Part I. Nonuniform mesh grids. *Journal of Computational Physics* 1996; **129**:357–363.
44. He XY, Luo LS, Dembo M. Some progress in the lattice Boltzmann method: Reynolds number enhancement in simulations. *Physica A: Statistical Mechanics and its Applications* 1997; **239**:276–285.
45. Mei CC. *The Applied Dynamics of Ocean Surface Waves*. World Scientific Publishing: Singapore, 1983; 285–287.
46. Guo Z, Zheng C. Analysis of lattice Boltzmann equation for microscale gas flows: relaxation times, boundary conditions and the Knudsen layer. *International Journal of Computational Fluid Dynamics* 2008; **22**:465–473.
47. Du R, Shi BC, Chen XW. Multi-relaxation-time lattice boltzmann model for incompressible flow. *Physics Letters A* 2006; **359**:564–572.
48. He XY, Zou QS, Luo LS, Dembo M. Analytic solutions of simple flow and analysis of nonslip boundary conditions for the lattice Boltzmann BGK model. *Journal of Statistical Physics* 1997; **87**:115–136.
49. Guo ZL, Zheng CG. *Theory and Applications of Lattice Boltzmann Method*. Science Press: Beijing, China, 2008; 63.
50. Guo ZL, Zheng CG, Shi BC. Non-equilibrium extrapolation method for velocity and pressure boundary conditions in the lattice Boltzmann method. *Chinese Physics* 2002; **11**:366–374.
51. Guo ZL, Zheng CG. *Theory and Applications of Lattice Boltzmann Method*. Science Press: Beijing, China, 2008; 45.
52. Lamb H. *Hydrodynamics*. Dover Publications: New York, USA, 1945.
53. Yuan HL, Wu CH. An implicit three-dimensional fully non-hydrostatic model for free-surface flows. *Journal for Numerical Methods in Fluids* 2004; **46**:709–733.
54. Wang K, Kang HG. Efficient computation method for two-dimensional nonlinear waves. *Acta Oceanologica Sinica* 2001; **20**:281–297.
55. Beji S, Battjes JA. Numerical simulation of nonlinear wave propagation over a bar. *Coastal Engineering* 1994; **23**:1–16.
56. He Y, Wang Y, Li Q. *Lattice Boltzmann Method: Theory and Applications*. Science Press: Beijing, China, 2008; 217–222.
57. Mehl M, Neckel T, Neumann P. Navier–Stokes and lattice-Boltzmann on octree-like grids in the Peano framework. *International Journal for Numerical Methods in Fluids* 2011; **65**:67–86.
58. Holme R, Rothman DH. Lattice-gas and lattice-Boltzmann models of miscible fluids. *Journal of Statistical Physics* 1992; **68**:409.